

High-angular resolution observations of methanol in the infrared dark cloud core G11.11-0.12P1[★]

Laura Gómez^{1,★★}, Friedrich Wyrowski¹, Thushara Pillai², Silvia Leurini¹, and Karl M. Menten¹

¹ Max-Planck-Institut für Radioastronomie, Auf dem Hügel 69, D-53121 Bonn, Germany
e-mail: [lgomez, wyrowski, sleurini, kmenten]@mpifr.de

² California Institute of Technology, MC 249-17, 1200 East California Boulevard, Pasadena, CA 91125, USA
e-mail: tpillai@astro.caltech.edu

Received ; accepted

ABSTRACT

Recent studies suggest that infrared dark clouds (IRDCs) have the potential of harboring the earliest stages of massive star formation and indeed evidence for this is found toward distinct regions within them. We present a study with the Plateau de Bure Interferometer of a core in the archetypal filamentary IRDC G11.11-0.12 at few arcsecond resolution to determine its physical and chemical structure. The data consist of continuum and line observations covering the C³⁴S 2 → 1 line and the methanol 2_k → 1_k v_t = 0 lines at 3mm and the methanol 5_k → 4_k v_t = 0 lines at 1mm. Our observations show extended emission in the continuum at 1 and 3 mm. The methanol 2_k → 1_k v_t = 0 emission presents three maxima extending over 1 pc scale (when merged with single-dish short-spacing observations); one of the maxima is spatially coincident with the continuum emission. The fitting results show enhanced methanol fractional abundance ($\sim 3 \times 10^{-8}$) at the central peak with respect to the other two peaks, where it decreases by about an order of magnitude ($\sim 4\text{--}6 \times 10^{-9}$). Evidence of extended 4.5 μ m emission, “wings” in the CH₃OH 2_k → 1_k spectra, and CH₃OH abundance enhancement point to the presence of an outflow in the East-West direction. In addition, we find a gradient of $\sim 4 \text{ km s}^{-1}$ in the same direction, which we interpret as being produced by an outflow(s)-cloud interaction.

Key words. ISM: abundances – ISM: individual objects (G11.11-0.12) – ISM: molecules – stars: formation – techniques: interferometric

1. Introduction

The objects now termed Infrared Dark Clouds (IRDCs) were first identified by Perault et al. (1996) and Egan et al. (1998) in images of the Galactic plane made with the *Infrared Space Observatory* (ISO) and the *Midcourse Space Experiment* (MSX) satellite, respectively. IRDCs have significant extinctions even at 8 and 15 μ m and are, thus, seen in silhouette against the bright, diffuse, mid-infrared Galactic emission. Millimeter and (sub)millimeter molecular studies reveal that some clumps within IRDCs have column densities of $> 10^{23} \text{ cm}^{-2}$, volume gas densities of $n > 10^5 \text{ cm}^{-3}$, and temperatures $T < 20 \text{ K}$ (e.g., Carey et al. 1998; Pillai et al. 2006a). Several studies suggest that IRDCs have the potential of harboring the earliest stages of massive star formation and indeed evidence for this is found toward distinct regions within them (Rathborne et al. 2005; Pillai et al. 2006b; Wang et al. 2006).

Pillai et al. (2006a) mapped the (J, K) = (1,1) and (2,2) inversion transitions of ammonia (NH₃) in the IRDC G11.11-0.12 with the Effelsberg 100m telescope and found gas temperatures of the order of 15 K for several clumps within this cloud. The left panel of Fig. 1 shows an overview of the region. Furthermore, Pillai et al. (2006b) reported the detection of 6.7 GHz class II methanol (CH₃OH) and 22.2 GHz water (H₂O) masers in the

IRDC Core G11.11-0.12P1 (hereafter G11.11P1). Both CH₃OH and H₂O masers are known as tracers of massive star formation. They found that these masers were associated with a SCUBA dust continuum peak (P1; Carey et al. 2000) and ascribed the kinematics of the methanol masing spots to a maser amplification from a Keplerian disk.

Recently, Henning et al. (2010) observed this filamentary IRDC with the PACS (at 70, 100, and 160 μ m) and the SPIRE (250, 350, and 500 μ m) instruments on board of the *Herschel Space Observatory*, with resolutions in the range of $\sim 6''\text{--}40''$. For G11.11P1, they obtain from a modified blackbody fit to the PACS data, a dust temperature of 24 K, a luminosity of 1346 L_{\odot} , and a mass of 240 M_{\odot} . Pillai et al. (2006a) and Leurini et al. (2007b) have used a two-component model to fit single-dish observations of NH₃ and CH₃OH spectra, respectively, and derived temperatures of $\sim 15\text{--}18 \text{ K}$ for the extended component (with size of $\sim 20''$ corresponding to 0.35 pc) and $\sim 47\text{--}60 \text{ K}$ for the inner component (with a size of $\sim 3''$ corresponding to 0.05 pc).

Methanol, which is a slightly asymmetric top molecule, has been used to derive physical parameters such as density and temperature in IRDCs (Leurini et al. 2007b), high-mass protostellar objects (e.g., Leurini et al. 2007a), massive young stars (e.g., van der Tak et al. 2000) as well as in low-mass protostellar systems (Kristensen et al. 2010). In particular, van der Tak et al. (2000) carried out a study toward 13 massive star-forming regions and found three types of CH₃OH abundance ($X_{\text{CH}_3\text{OH}} \equiv N_{\text{CH}_3\text{OH}}/N_{\text{H}_2}$) profiles: $X_{\text{CH}_3\text{OH}} \sim 10^{-9}$ for the coldest sources, from 10^{-9} to 10^{-7} for warmer sources, and 10^{-7} for hot cores. CH₃OH has also been associated with outflows where the methanol abundance enhancements have been found to be a fac-

[★] Based on observations carried out with the IRAM Plateau de Bure Interferometer and the IRAM 30m telescope. IRAM is supported by INSU/CNRS (France), MPG (Germany), and IGN (Spain).

^{★★} Member of the International Max Planck Research School (IMPRS) for Astronomy and Astrophysics at the Universities of Bonn and Cologne.

tor as large as 400-1 000 (e.g., Bachiller et al. 1995; Garay et al. 2002; Kristensen et al. 2010).

In this paper, we present arcsecond resolution millimeter continuum and line observations toward G11.11P1 with the aim to determining its physical and chemical structure. In Sect. 2, we describe our observations carried out with the IRAM Plateau de Bure Interferometer. In Sect. 3, we present continuum and line results together with the analysis. The discussion is presented in Sect. 4 and the summary is given in Sect. 5.

2. Observations and data reduction

2.1. IRAM PdBI observations

G11.11P1 was observed with the IRAM six element array Plateau de Bure Interferometer (PdBI; Guilloteau et al. 1992) in D and C configurations in 2005 and 2006, respectively.

During the 2006 observations, one antenna was equipped with the prototype New Generation Receiver. Because of a difference in the frequency scheme of this receiver, visibilities obtained in the image sideband in this antenna were discarded. The receivers were tuned single side-band at 3 mm and double side-band at 1 mm. The 3 mm receivers were centered at 96.64 GHz and the 1 mm receivers at 241.81 GHz (see Table 1). At 3 mm, the $C^{34}S$ $2 \rightarrow 1$ line and the CH_3OH $2_k \rightarrow 1_k$ $v_t = 0$ lines were covered by using two correlator units of 80 MHz with a spectral resolution of 0.3125 MHz (0.97 km s^{-1}) and by two correlator units of 320 MHz. The latter were used, free of line, to produce the continuum image with a total bandwidth of ~ 450 MHz. At 1 mm, the CH_3OH $5_k \rightarrow 4_k$ $v_t = 0$ lines were observed with two units of 160 MHz with a spectral resolution of 1.250 MHz (1.55 km s^{-1}). The remaining units of 80, 160, and 320 MHz were placed in such a way that a frequency range free of lines could be used to measure the continuum flux. The total bandwidth of both sidebands was ~ 700 MHz.

The phase and amplitude were calibrated with observations of the object 1730-130. The bandpass calibration was done with 3C 273. MWC 349 was used as primary flux calibrator of the 3 and 1 mm data (see Table 1). We estimate the final flux density accuracy to be $\sim 5\%$ and 10% for the 3mm and 1mm data, respectively. Continuum images were subtracted from the line data in the visibility plane. The combination of the C and D configurations provides angular scales from $1''.8$ – $12''.6$ (1 mm) and $4''.4$ – $32''.5$ (3 mm), i.e., providing information on spatial scales of 0.03–0.22 pc and 0.08–0.57 pc, respectively.

The calibration and data reduction were made within the GILDAS package¹ at IRAM Grenoble. Images were created with natural weighting and CLEANed using the standard Högbom algorithm.

2.2. IRAM 30m short-spacing observations

G11.11P1 was observed in the $2_k \rightarrow 1_k$ $v_t = 0$ (3 mm) and $5_k \rightarrow 4_k$ (1 mm) CH_3OH bands with the IRAM 30m telescope. An area of $90'' \times 90''$ was mapped with the SIS B100 receiver at 3 mm and $66'' \times 66''$ with the HERA receiver (Schuster et al. 2004) at 1 mm with a bandwidth of ~ 140 MHz. Sampling at 3 mm was of $15''$ while at 1 mm was of $6''$. Conversion from antenna temperature to main-beam brightness temperature (T_{MB}) was performed by using a beam efficiency of 0.78 at 3 mm and 0.52 at 1 mm. The *rms* at 1 mm is 0.3 K and at 3 mm is 0.02 K. The data were

Table 1. Parameters for the IRAM PdBI observations.

Parameter	Value
Pointing center	R.A. (J2000) = $18^h 10^m 28^s.24$ Decl. (J2000) = $-19^\circ 22' 30''.5$
Number of antennas	6
Baseline range	24–176 m
Band center	96.64 and 241.81 GHz
Primary HPBW	$52''$ at 96.64 GHz $21''$ at 241.81 GHz
Synthesised HPBW	$6''.0 \times 3''.1$ at 96.64 GHz $2''.6 \times 1''.1$ at 241.81 GHz
Primary flux density calibrator:	1.17 Jy at 96.64 GHz
MWC349	2.03 Jy at 241.81 GHz

reduced with the CLASS program, part of the GILDAS software package.

The 3 mm single-dish data are used to create short-spacing pseudo-visibilities; these are then merged with the interferometric observations. All data are imaged and deconvolved together. The processing was performed in GILDAS/MAPPING following standard procedures of the UV_SHORT task (see Rodríguez-Fernández et al. 2008² for details on the pseudo-visibility technique). In Sect. 3.3 we present the result of recovering the short-spacing information for the 3 mm data.

Unfortunately, we were not able to merge the interferometric and single-dish observations for the 1 mm data due to poor signal-to-noise ratio of the latter data. However, we make use of the 1 mm single-dish data in the following sections to help in the analysis and interpretation of this core.

3. Results and Analysis

3.1. PdBI: Continuum emission

3.1.1. Morphology and core size

The *right* panel of Fig. 1 presents the continuum images at 1 and 3 mm of G11.11P1. At the resolution of both images, the emission is extended; the peak intensity positions coincide with each other and with the maser positions as well. The morphology at 3 mm resembles that previously imaged with the Berkeley-Illinois-Maryland-Association (BIMA) interferometer by Pillai et al. (2006b) with a slightly lower resolution ($8''.3 \times 3''.9$).

In Table 2 we list the parameters of the continuum emission. Deconvolved sizes have been obtained by fitting two-dimensional Gaussians to the continuum maps and yielding a core size of $\sim 0.16 \text{ pc} \times 0.08 \text{ pc}$ with a PA 24° at 3 mm and $\sim 0.09 \text{ pc} \times 0.07 \text{ pc}$ with a PA 165° at 1 mm. We have assumed a kinematic distance of 3.6 kpc.

3.1.2. Mass

Assuming that the mm continuum is mainly due to optically thin dust emission, we estimate the gas mass, M_g , by using the following expression (Hildebrand 1983)

$$M_g = \frac{F_\nu D^2 R_{gd}}{\kappa_\nu B_\nu(T_d)} M_\odot, \quad (1)$$

² http://iram.fr/GENERAL/reports/IRAM_memo_2008-2-short-spacings.pdf

¹ <http://www.iram.fr/IRAMFR/GILDAS>

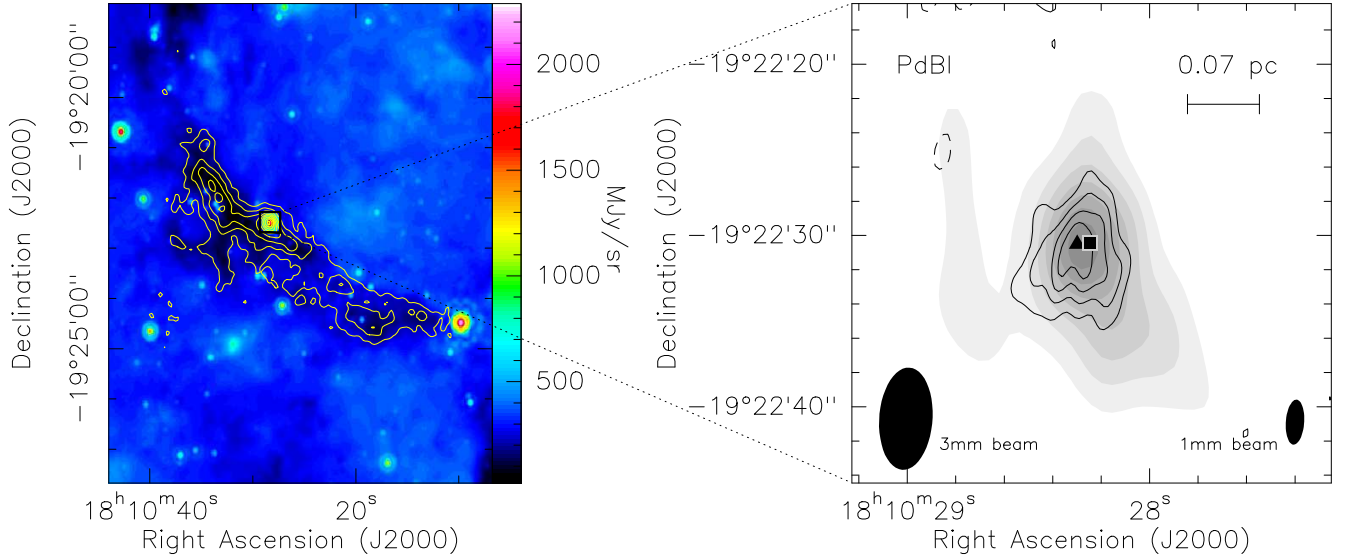


Fig. 1. *Left:* SCUBA 850 μm (Carey et al. 2000) contours overlaid on the MIPS GAL 24 μm image of the IRDC G11.11-0.12. *Right:* PdBI 1.2 mm continuum emission (contours) of G11.11P1 overlaid on the 3.1 mm continuum emission (grey scale image). First contour and contour spacing for the 3.1 mm emission are 0.9 mJy beam $^{-1}$ (3σ), the dotted contours show the negative emission (-3σ); the synthesized beam ($6''.0 \times 3''.1$; PA = 176°) is shown in the bottom left corner. First contour and contour spacing for the 1.2 mm emission are 6.3 mJy beam $^{-1}$ (3σ), the dashed contours show the negative emission (-3σ); the synthesized beam ($2''.6 \times 1''.1$; PA = 176°) is shown in the bottom right corner. The filled triangle at R.A. = $18^{\text{h}}10^{\text{m}}28^{\text{s}}.29$, Decl. = $-19^\circ22'30''.5$ and the filled square at R.A. = $18^{\text{h}}10^{\text{m}}28^{\text{s}}.25$, Decl. = $-19^\circ22'30''.45$ (J2000) indicate the water and (integrated emission) methanol masers, respectively, reported by Pillai et al. (2006b).

Table 2. Parameters of the observed continuum emission.

Frequency (GHz)	Peak Intensity Position R.A. (J2000) Decl. (J2000)	Peak Intensity (mJy beam $^{-1}$)	Flux density ^a (mJy)	Deconvolved angular size ^b	Mass ^c (M_\odot)
96.7	$18^{\text{h}}10^{\text{m}}28^{\text{s}}.28$ $-19^\circ22'30''.5$	7.0	20.2	$(8''.9 \pm 0''.6) \times (4''.4 \pm 0''.5)$; $+24^\circ \pm 7^\circ$	37
241.8	$18^{\text{h}}10^{\text{m}}28^{\text{s}}.29$ $-19^\circ22'30''.5$	30.8	208.6	$(4''.9 \pm 0''.6) \times (3''.9 \pm 0''.5)$; $+165^\circ \pm 36^\circ$	13

^a Flux density was obtained by summing the continuum emission above 3σ level within a polygon encompassing the core.

^b Major axis \times minor axis, at FWHM; position angle of major axis from fits of elliptical Gaussian.

^c Assuming a distance of 3.6 kpc and dust temperature of 60 K.

where F_ν is the observed integrated flux density in Jy, D is the distance, R_{gd} is the gas-to-dust mass ratio, κ_ν is the dust opacity coefficient, and $B_\nu(T_d)$ is the Planck function at the dust temperature (T_d). The 1 mm flux density was obtained by summing the 1 mm continuum emission above 3σ (> 6 mJy beam $^{-1}$) level within a polygon encompassing the core; the integrated flux density is ~ 209 mJy. We assume a gas-to-dust mass ratio of 100, and adopt a $\kappa_\nu = 1$ cm 2 g $^{-1}$ (Ossenkopf & Henning 1994), at 1mm, for an MRN (Mathis et al. 1977) graphite-silicate grain mixture with thick ice mantles, at a gas density of 10^6 cm $^{-3}$. If we use $T_d = 60$ K (Laurini et al. 2007b; Pillai et al. 2006a), a proper temperature for a region where methanol emission is arising, a mass of $13 M_\odot$ at 1 mm is obtained for G11.11P1 (see Table 2). This is equivalent to adopt a dust opacity coefficient $k_\nu = 0.1$ ($\nu/10^{12}$ Hz) $^\beta$ (Beckwith et al. 1990), which includes the gas contribution to the total mass for a $R_{\text{gd}} = 100$, with $\beta = 1.6$. Given the uncertainties in the models of dust opacities and variation of the gas-to-dust ratio, β is within the errors comparable to the upper limit we obtain in Sect. 3.1.3.

Comparing the flux from the Bolocam Galactic Plane Survey (BGPS³; Aguirre et al. 2011) 1.1 mm with the PdBI 1.2 mm con-

tinuum flux we find that the interferometric observations filter out about 75% of the emission.

To make a rough mass estimate of the core from the 3 mm data, all parameters remain the same as with the 1 mm data except for the flux density, ~ 20 mJy, and $\kappa_\nu = 0.2$ cm 2 g $^{-1}$ (extrapolating from Table 1 Column 9 in Ossenkopf & Henning 1994). We obtain a core mass of $37 M_\odot$.

3.1.3. Density, temperature, and spectral indices

For deeper insight into the source structure, we have analyzed the 1 mm and 3 mm continuum data in the u - v domain avoiding the cleaning and u - v sampling effects. Figure 2 shows the averaged amplitudes averaged over a concentric annulus (from the continuum peak positions) versus deprojected u - v distance in units of wavelength. The amplitudes have been averaged vectorially and the 3 mm u - v amplitudes in Jy were scaled by a factor of 15 to match the 1 mm visibilities. Error bars are 1σ statistical errors based on the standard deviation of the mean of the data points in the bin.

Since the index of the power law in u - v distance is related to the index of the power law in radial distance, r , following

³ http://irsa.ipac.caltech.edu/data/BOLOCAM_GPS/

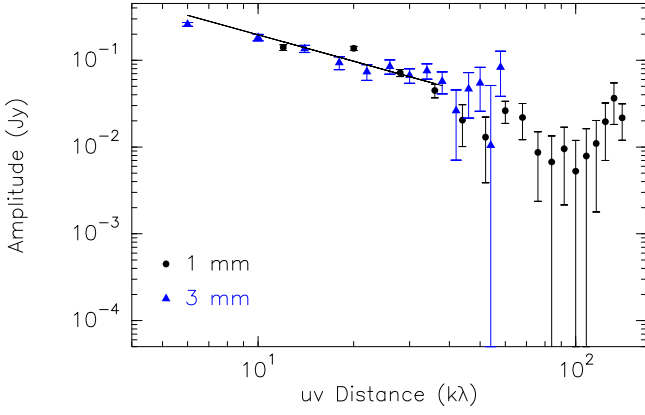


Fig. 2. Continuum emission from G11.11P1 at 3.1 mm (filled triangles) and 1.2 mm (filled circles) in the Fourier domain. Amplitudes are averaged in bins of deprojected u - v distance from the continuum intensity peaks. The 3.1 mm u - v amplitudes have been scaled by a factor of 15. The straight solid line represents the least-squares fit to the data. Error bars are for 1σ statistical errors based on the standard deviation of the mean of the data points in the bin.

Looney et al. (2003), we can write $F(r) \propto r^{-(p+q)+1} \rightarrow V(s) \propto s^{(p+q)-3}$, where $F(r)$ is the flux density in the image domain, $V(s)$ is the Fourier transform of the flux density, s is u - v distance and, p and q are the power-law indices of the density ($n \propto r^{-p}$) and temperature structure ($T \propto r^{-q}$), respectively.

The least-squares fit (see Fig. 2) to both the 1 mm and 3 mm data yields a slope of -1.01 ± 0.02 , corresponding to $p + q \sim 2.0$. Points starting at 40 kλ, which corresponds to an angular scale of $\sim 6''$ (0.1 pc), were excluded from the fit because the signal-to-noise ratio gets very low. If the index $q = 0.4$ (Goldreich & Kwan 1974), the density profile index is 1.6.

We estimate a mean volume gas density of the core ($n = \frac{M_g}{\frac{4}{3}\pi R^3 \mu_{H_2} m_H}$, where R is the core radius) of $7 \times 10^5 \text{ cm}^{-3}$ using the mass derived from the dust observations at 1 mm ($13 M_\odot$) and the geometric mean of the deconvolved linear size as the core radius ($R = \sqrt{(FWHM_{\text{maj}}/2) \times (FWHM_{\text{min}}/2)} = 0.04 \text{ pc}$).

The scaling factor of 15 corresponds to a spectral index $\alpha = 3.0 \pm 0.4$ and we thus obtain an opacity spectral index $\beta = 1.0 \pm 0.4$. The derived dust opacity index corresponds, taking the upper limit, to a “normal” interstellar dust material value. Nonetheless, if taking the lower limit, the dust opacity index goes down to a value that is usually found toward disks (e.g., Beckwith & Sargent 1991; Natta et al. 2004), which has been ascribed to grain growth. Alternatively, the presence of winds/outflows (see Sect. 4.2) could mimic a low value of β (Beuther et al. 2007). Here we adopt a $\beta = 1.6$ in the rest of the paper.

3.2. PdBI: Molecular emission

Spectroscopic parameters of the detected $\text{C}^{34}\text{S } 2 \rightarrow 1$ and $\text{CH}_3\text{OH } 2_k \rightarrow 1_k$ and $5_k \rightarrow 4_k$ transitions toward G11.11P1 are listed in Table 3. The interferometric integrated intensity maps, overlaid on their corresponding continuum emission, along with sample spectra are presented in Figs. 3–5.

Table 3. Molecular parameters of detected line transitions.

Molecule ^a	Transition	Frequency (MHz)	E_u/k (K)	$\mu^2 S$ (D ²)
C^{34}S	$2 \rightarrow 1$	96412.9495	6.94	7.6678
CH_3OH	$2_{-1} \rightarrow 1_{-1} E$	96739.3620	12.55	1.2134
	$2_0 \rightarrow 1_0 A$	96741.3750	6.97	1.6170
	$2_0 \rightarrow 1_0 E$	96744.5500	20.10	1.6166
	$2_1 \rightarrow 1_1 E$	96755.5110	28.03	1.2442
	$5_0 \rightarrow 4_0 E$	241700.2190	47.96	4.0402
	$5_{-1} \rightarrow 4_{-1} E$	241767.2240	40.41	3.8824
	$5_0 \rightarrow 4_0 A$	241791.4310	34.83	4.0430
	$5_{\pm 3} \rightarrow 4_{\pm 3} A$	241832.9100	84.68	2.5775
	$5_1 \rightarrow 4_1 E$	241879.0730	55.91	3.9802
	$5_{-2} \rightarrow 4_{-2} E$	241904.1520 ^b	60.76	3.3986
	$5_2 \rightarrow 4_2 E$	241904.6450 ^b	57.11	3.3558

^a Rest frequencies, upper level energies and $\mu^2 S$ from the Cologne Database for Molecular Spectroscopy (CDMS; Müller et al. 2001, 2005) as of December 2010.

^b Blend of lines.

3.2.1. C^{34}S emission

The integrated intensity map of the $\text{C}^{34}\text{S } 2 \rightarrow 1$ line, is shown in the *top* panel of Fig. 3. This emission is spatially coincident with the 3 mm continuum; moreover, some weaker emission (at 3σ level) extends along the E-W direction. Observed parameters toward the peak position in the integrated intensity map are presented in Table 4.

Virial mass. The virial mass of a core with a power-law density distribution is $M_{\text{vir}} = k_1 \sigma_v^2 R / G$ (MacLaren et al. 1988) where $k_1 = (5 - 2p)/(3 - p)$, σ_v is the three-dimensional root-mean-square velocity which is related to the FWHM line width, ΔV , through $\sigma_v^2 = (3/8 \ln 2) \Delta V^2$, R is the core radius and G is the Gravitational constant. For $p = 1.6$ (see Sect. 3.1.3), the virial mass can be expressed as

$$M_{\text{vir}} \simeq 161 \times \left(\frac{R}{\text{pc}} \right) \left(\frac{\Delta V}{\text{km s}^{-1}} \right)^2 M_\odot. \quad (2)$$

A virial mass of $\sim 135 M_\odot$ is calculated when using $\Delta V = 4.1 \text{ km s}^{-1}$ (see Table 4) of the C^{34}S optically thin line and $R = 0.05 \text{ pc}$, which corresponds the geometric mean of the deconvolved linear size.

Virial parameter. The virial parameter (Bertoldi & McKee 1992) for a spherical cloud is defined as $\alpha_{\text{vir}} \equiv M_{\text{vir}}/M_{\text{tot}}$, where M_{tot} is the total mass. If we assume that $M_{\text{tot}} = M_g = 37 M_\odot$, then $\alpha_{\text{vir}} = 3.6$.

It is worth noting that the C^{34}S line width could be affected by unbound motions, e.g., outflows, partially broadening the line and thereby increasing the virial mass estimate significantly and the virial parameter as well.

Jeans mass. Following Stahler & Palla (2005), we can calculate the Jeans mass

$$M_J = \frac{ma^3}{\rho^{1/2} G^{3/2}} \simeq 1.0 \times \left(\frac{T}{10 \text{ K}} \right)^{3/2} \left(\frac{n}{10^4 \text{ cm}^{-3}} \right)^{-1/2} M_\odot, \quad (3)$$

where a is the isothermal sound speed and ρ is the mass density. For $n = 7 \times 10^5 \text{ cm}^{-3}$ (see Sect. 3.1.3) and $T = 60 \text{ K}$, we obtain a Jeans mass of $\sim 1.8 M_\odot$. We find a gas mass (M_g) to the Jeans mass (M_J) ratio larger than unity; other interferometric studies (Rathborne et al. 2008; Zhang et al. 2009) toward IRDCs report $M_g/M_J > 1$ as well.

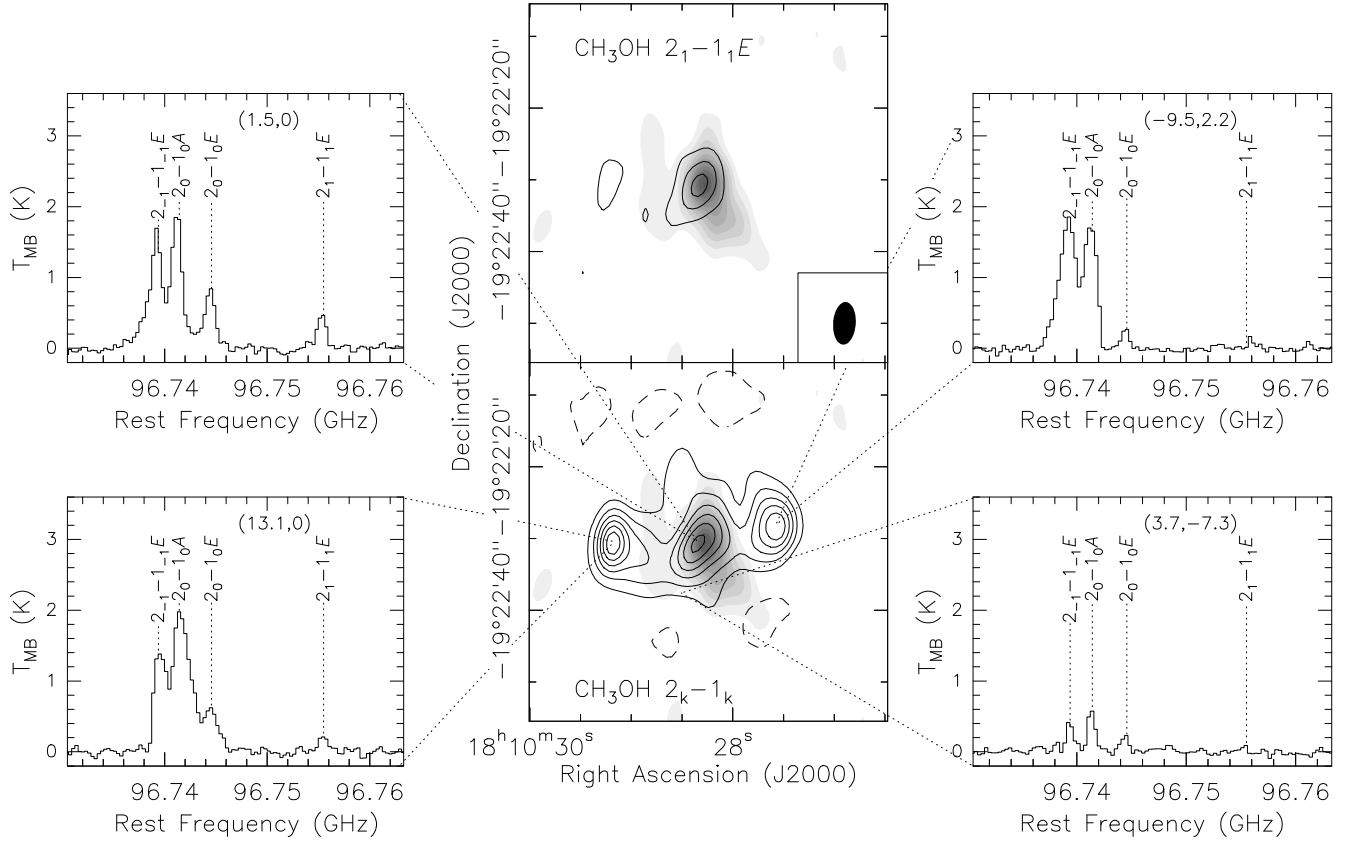


Fig. 4. In grey-scale the 3.1 mm continuum emission of G11.11P1. *Top middle:* Contour image of the CH₃OH emission integrated under the line $2_1 \rightarrow 1_1 E$. First contour and contour spacing are $0.66 \text{ Jy beam}^{-1} \text{ km s}^{-1}$ (3σ). The synthesized beam ($6''.0 \times 3''.2$; PA = 174°) is shown in the lower right corner. *Bottom middle:* Contour image of the CH₃OH emission integrated under the $2_{-1} \rightarrow 1_{-1} E$, $2_0 \rightarrow 1_0 A$, and $2_0 \rightarrow 1_0 E$ transition lines. First contour and contour spacing are $0.45 \text{ Jy beam}^{-1} \text{ km s}^{-1}$ (3σ). The dashed contours show the negative emission (-3σ). Shown are also spectra at four different positions; positions are given in each inset in parenthesis in units of arcsec.

Table 4. Observed molecular line parameters from Gaussian fits.

Molecule	Transition	v_{LSR} (km s^{-1})	Peak T_{MB} (K)	ΔV (FWHM) (km s^{-1})	$\int T_{\text{MB}} dV$ (K km s^{-1})
Offset ($0'', 0''$)					
C ³⁴ S	$2 \rightarrow 1$	29.90 (0.04)	1.31 (0.04)	4.1 (0.1)	5.6 (0.1)
Offset ($1''.5, 0''$)					
CH ₃ OH	$2_{-1} \rightarrow 1_{-1} E$	29.85 (0.05)	1.49 (0.04)	5.1 (0.2)	8.0 (0.2)
	$2_0 \rightarrow 1_0 A$	29.72 (0.04)	1.89 (0.04)	3.6 (0.1)	7.3 (0.2)
	$2_0 \rightarrow 1_0 E$	29.87 (0.09)	0.78 (0.04)	4.4 (0.2)	3.6 (0.1)
	$2_1 \rightarrow 1_1 E$	29.79 (0.01)	0.49 (0.04)	3.1 (0.2)	1.6 (0.1)
	$5_0 \rightarrow 4_0 E$	29.71 (0.20)	0.70 (0.04)	4.1 (0.5)	3.1 (0.3)
	$5_{-1} \rightarrow 4_{-1} E$	29.92 (0.09)	1.48 (0.04)	4.1 (0.2)	6.5 (0.3)
	$5_0 \rightarrow 4_0 A$	30.00 (0.05)	1.80 (0.04)	4.3 (0.2)	8.3 (0.3)
	$5_1 \rightarrow 4_1 E$	29.78 (0.41)	0.33 (0.04)	3.9 (1.3)	1.4 (0.3)

Notes. CH₃OH $2_k \rightarrow 1_k$ and $5_k \rightarrow 4_k$ line parameters listed in this table were used in the rotational diagram method described in the text. The CH₃OH $5_k \rightarrow 4_k$ transitions have been convolved to the $2_k \rightarrow 1_k$ resolution.

From our interferometric observations at 1mm, and taking a flux density equal to the 3σ detection level, we derive a mass sensitivity limit of $0.4 M_\odot$. Comparing this value with the Jeans mass, we note that our mass sensitivity limit is good enough to detect fragments of the order of the Jeans mass.

3.2.2. CH₃OH emission

Figure 4 shows the integrated intensity map of the CH₃OH $2_k \rightarrow 1_k$ quartet of lines (*bottom middle*). This emission presents three maxima; one of them is spatially coincident with the 1 and 3 mm continuum emission which peaks at ($1''.5, 0''$), the other two are located at ($13''.1, 0''$) and ($-9''.5, 2''.2$). We plot sample spectra at four different positions, including the three max-

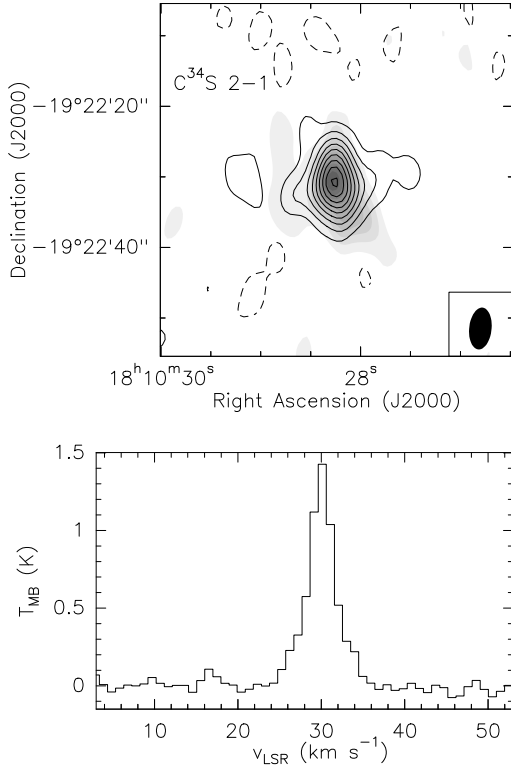


Fig. 3. *Top:* Contour image of the emission integrated under the $C^{34}S$ $2 \rightarrow 1$ line, in the velocity range from 22.4 to 37.9 km s^{-1} , overlaid on the grey-scale 3.1 mm continuum emission of G11.11P1. First contour and contour spacing are $0.09 \text{ Jy beam}^{-1} \text{ km s}^{-1}$ (3σ), the dashed contours show the negative emission (-3σ). The synthesized beam ($6''.0 \times 3''.2$; PA = 176°) is shown in the lower right corner. *Bottom:* Spectrum of $C^{34}S$ $2 \rightarrow 1$ toward the peak position on the integrated intensity map: R.A. = $18^{\text{h}}10^{\text{m}}28^{\text{s}}.24$, Decl. = $-19^\circ22'30''.5$ (J2000).

ima and one position on the envelope ($3''.7, -7''.3$), in order to compare line profiles, absolute line strengths, and the relative strengths among lines. The high excitation CH_3OH $2_1 \rightarrow 1_1E$ transition that arises from a smaller region is also shown (*top middle*).

Line widths at and close to the three peak positions are, in average $\sim 5 \text{ km s}^{-1}$ with line profiles showing red- and/or blueshifted “wings”, while in the outer parts of the envelope, e.g., at the ($3''.7, -7''.3$) position, the line width is narrower ($\sim 2 \text{ km s}^{-1}$; see spectra in Fig. 4).

In Fig. 5 we present the integrated intensity map of the strongest line CH_3OH $5_0 \rightarrow 4_0A$. The emission distribution is as extended as that of the 1 mm continuum and the CH_3OH $2_1 \rightarrow 1_1E$ emissions.

Local thermodynamic equilibrium (LTE) analysis. We derived the rotational temperatures and methanol column densities by using the rotational diagram method (e.g., Cummins et al. 1986; Goldsmith & Langer 1999). Briefly, for an optically thin line, the column density in the upper level (N_u) can be written as $N_u = 3kW/(8\pi^3\nu S\mu^2)$, where k is the Boltzmann constant, W is the integrated intensity of a line ($\int T_{\text{MB}} dV$), ν the frequency, S the line strength, μ the dipole moment. Under LTE conditions, the population of each level follows a Boltzmann law at the gas temperature T by $N_u = (N/Q)g_u e^{-E_u/kT}$, where N is the total column density, Q the partition function, and g_u and E_u are the

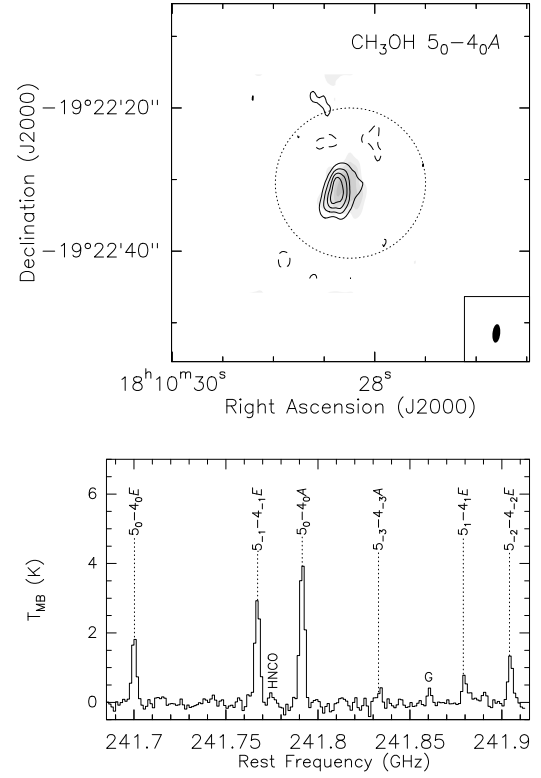


Fig. 5. *Top:* Contour image of the emission integrated under the $5_0 \rightarrow 4_0A$ transition line, overlaid on the grey-scale 1.2 mm continuum emission of G11.11P1. First contour and contour spacing are $0.16 \text{ Jy beam}^{-1} \text{ km s}^{-1}$ (3σ); the dashed contours show the negative emission (-3σ). The synthesized beam ($2''.6 \times 1''.1$; PA = 174°) is shown in the lower right corner. The dotted circle indicates the interferometer primary beam ($21''$) at this frequency. *Bottom:* Spectrum of CH_3OH $5_k \rightarrow 4_k$ towards the position: R.A. = $18^{\text{h}}10^{\text{m}}28^{\text{s}}.40$, Decl. = $-19^\circ22'31''.9$ (J2000). The HNCO $11_{0,11} \rightarrow 10_{0,10}$ line (at 241774.0320 MHz with $E_u/k = 69.67 \text{ K}$ and $\mu^2 S = 27.4590 \text{ D}^2$) is shown as well. The “G” shows an artifact produced in the central channels of a correlator unit due to Gibbs effect.

statistical weight and the energy of the upper level, respectively. We then obtain

$$\log\left(\frac{N_u}{g_u}\right) = \log\left(\frac{N}{Q}\right) - \frac{\log e E_u}{T k}. \quad (4)$$

Using Eq. 4, we plot $\log(N_u/g_u)$ versus E_u/k (see Fig. 6) and make a least-squares fit for T and N taking into account both CH_3OH $2_k \rightarrow 1_k$ and $5_k \rightarrow 4_k$ bands. The partition function of CH_3OH is $Q = 2[\frac{\pi(kT)^3}{h^3 ABC}]^{1/2}$ (Turner 1991), where h is the Planck constant and A , B , and C are the rotation constants (CDMS; Müller et al. 2001, 2005). A $Q = 1.23 T^{1.5}$ was used in the calculations. The CH_3OH $5_k \rightarrow 4_k$ data were smoothed to the resolution of the $2_k \rightarrow 1_k$ data. CH_3OH transition lines that were used in this fit are listed in Table 4.

To estimate the CH_3OH fractional abundance (relative to H_2), $X_{\text{CH}_3\text{OH}}$, we calculate the beam-averaged H_2 column density, N_{H_2} , following the expression

$$N_{\text{H}_2} = \frac{I_{\nu}^{\text{peak}} R_{\text{gd}}}{\kappa_{\nu} B_{\nu}(T_d) \Omega \mu_{\text{H}_2} m_{\text{H}}} \text{ cm}^{-2}, \quad (5)$$

where I_{ν}^{peak} is the peak intensity in Jy/beam , $\mu_{\text{H}_2} = 2.8$ (Kauffmann et al. 2008) is the molecular weight per hydrogen

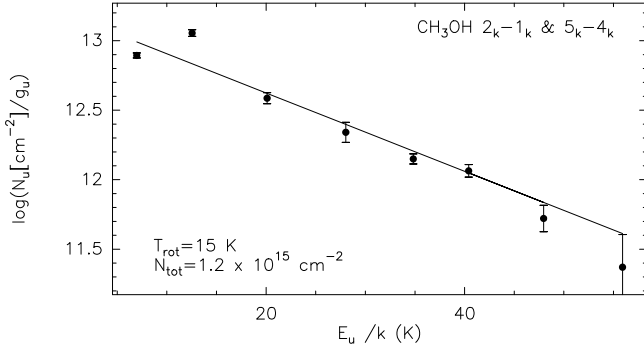


Fig. 6. Rotational diagram of CH₃OH (2–1) and (5–4) transition lines towards the (1′′5, 0′′) position. The straight line is a least-squares fit to the data corresponding to the rotational temperature and column densities indicated in the bottom left. Error bars are for 1 σ uncertainties.

molecule, and $\Omega = (\pi\theta_{\min}\theta_{\text{maj}})/(4\ln 2)$ is the beam solid angle of an elliptical Gaussian beam with minor and major axes θ_{\min} and θ_{maj} , respectively.

We obtained a rotational temperature of 15 K and a CH₃OH column density, $N_{\text{CH}_3\text{OH}}$, of $1.2 \times 10^{15} \text{ cm}^{-2}$ towards the (1′′5, 0′′) peak position. Since the lines are likely sub-thermally excited, we take a dust temperature $T_d = 60 \text{ K}$ (see LVG analysis) and obtain a $N_{\text{H}_2} = 4.6 \times 10^{22} \text{ cm}^{-2}$ (from our 1 mm continuum data convolved to the 3 mm data) and a $X_{\text{CH}_3\text{OH}}$ of 2.6×10^{-8} .

At the (13′′1, 0′′) position, we get a $X_{\text{CH}_3\text{OH}} = 3.7 \times 10^{-9}$, when using $N_{\text{CH}_3\text{OH}} = 2.9 \times 10^{14} \text{ cm}^{-2}$ and $N_{\text{H}_2} = 7.7 \times 10^{22} \text{ cm}^{-2}$. A rotational temperature of 13 K was calculated. At the (−9′′5, 2′′2) position, the values for the $X_{\text{CH}_3\text{OH}}$, $N_{\text{CH}_3\text{OH}}$, and N_{H_2} are: 5.6×10^{-9} , $3.8 \times 10^{14} \text{ cm}^{-2}$, and $6.8 \times 10^{22} \text{ cm}^{-2}$, respectively. For the (−9′′5, 2′′2) peak, we fixed $T = 15 \text{ K}$ because of low signal-to-noise of one of the three lines used in the fit. $N_{\text{CH}_3\text{OH}}$ for both peaks (13′′1, 0′′) and (−9′′5, 2′′2) were calculated from the 3 mm interferometric map only and N_{H_2} from the SCUBA 850 μm dust continuum; the interferometric observations were convolved to the SCUBA beam size (14′′).

Large velocity gradient (LVG) analysis. Leurini et al. (2004) found several ratios, from some CH₃OH-*E* transitions, to be calibration-independent tracers of density in the 1 and 3 mm bands. We have used their LVG calculations and have plotted the following integrated intensity line ratios: $5_0 \rightarrow 4_0/5_{-1} \rightarrow 4_{-1}$, $5_1 \rightarrow 4_1/5_{-1} \rightarrow 4_{-1}$, and $5_1 \rightarrow 4_1/5_0 \rightarrow 4_0$, in a temperature-density (T - n) plane. In Fig. 7, the observed ratios, towards the (1′′5, 0′′) position, are represented by the black dash-dotted line, blue solid line, and pink dashed line. The $2_k \rightarrow 1_k$ quartet of lines in the 3 mm band were not used in the analysis because they are blended.

Given the results for CH₃OH column densities in the LTE analysis, the explored LVG models for the excitation of methanol run for temperatures in the range of 10–200 K, for densities 10^5 – 10^8 cm^{-3} , and for two CH₃OH column densities per line width 10^{14} and $10^{15} \text{ cm}^{-2}/(\text{km s}^{-1})$.

For an average line width of 4 km s^{-1} , this corresponds to $N_{\text{CH}_3\text{OH-E}} = 4 \times 10^{14} \text{ cm}^{-2}$ and $4 \times 10^{15} \text{ cm}^{-2}$, respectively. Depending on the column density, two possible solutions are found: at $N_{\text{CH}_3\text{OH-E}} = 4 \times 10^{14} \text{ cm}^{-2}$, the three integrated intensity line ratios intercept at $T = 17 \text{ K}$ and $n = 10^7 \text{ cm}^{-3}$. On the other hand, at $N_{\text{CH}_3\text{OH-E}} = 4 \times 10^{15} \text{ cm}^{-2}$, the interception is at $T = 60 \text{ K}$ and $n = 2 \times 10^6 \text{ cm}^{-3}$ (see Fig. 7). The methanol column density inferred in this case is consistent with the LTE analysis within a factor of 3, but the intensities in

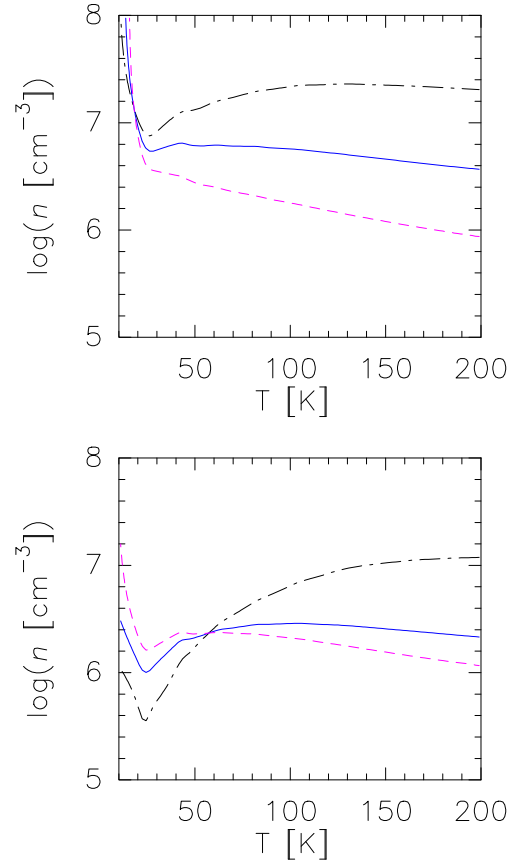


Fig. 7. Results of statistical equilibrium calculations for CH₃OH-*E*. The $5_0 \rightarrow 4_0/5_{-1} \rightarrow 4_{-1}$ (black dash-dotted line), $5_1 \rightarrow 4_1/5_{-1} \rightarrow 4_{-1}$ (blue solid line), and $5_1 \rightarrow 4_1/5_0 \rightarrow 4_0$ (pink dashed line) observed integrated intensity line ratios towards the (1′′5, 0′′) position in logarithmic scale are shown as function of H₂ density and temperature at $N_{\text{CH}_3\text{OH}}/\Delta V = 10^{14} \text{ cm}^{-2}/(\text{km s}^{-1})$ (top) and $N_{\text{CH}_3\text{OH}}/\Delta V = 10^{15} \text{ cm}^{-2}/(\text{km s}^{-1})$ (bottom).

this model are one order of magnitude higher than the observed line intensities. In other words, to fit the observations with the $N_{\text{CH}_3\text{OH-E}} = 4 \times 10^{15} \text{ cm}^{-2}$ model, we need a beam filling factor of 0.1 resulting in a more compact source (with a size of 0′′5 corresponding to 0.009 pc or 1800 AU), even smaller than the one modelled by Pillai et al. (2006a) and Leurini et al. (2007b).

To gain more insight into the possible T - n degeneracy, in Figure 8, we show n vs. $N_{\text{CH}_3\text{OH}}$ plots, at different temperatures (10–70 K), where the color-coding for the ratios (along with their 1 σ values) are the same as in Fig. 7; additionally, we show in each panel the peak main beam brightness temperature of the $5_0 \rightarrow 4_0E$ transition (green dotted line). The parameters obtained in the regions in the left side of the green dotted line imply beam filling factors greater than 1, which is not possible. In each panel, the areas of interest are those that lie in the right side of the green line and, at the same time, are delimited by the integrated intensity ratios (taking into account their 1 σ values). We see that, for T in the range 30–70 K, the n remains constant up to $N_{\text{CH}_3\text{OH}} \sim 4 \times 10^{14} \text{ cm}^{-2}$, while for the very low T ($= 10 \text{ K}$), there is no solution.

Given our density estimate from the dust continuum, we view the low T , high n solutions with a large filling factor as unlikely. Therefore, although we cannot strongly constrain the physical parameters of the gas emitting methanol from the LVG

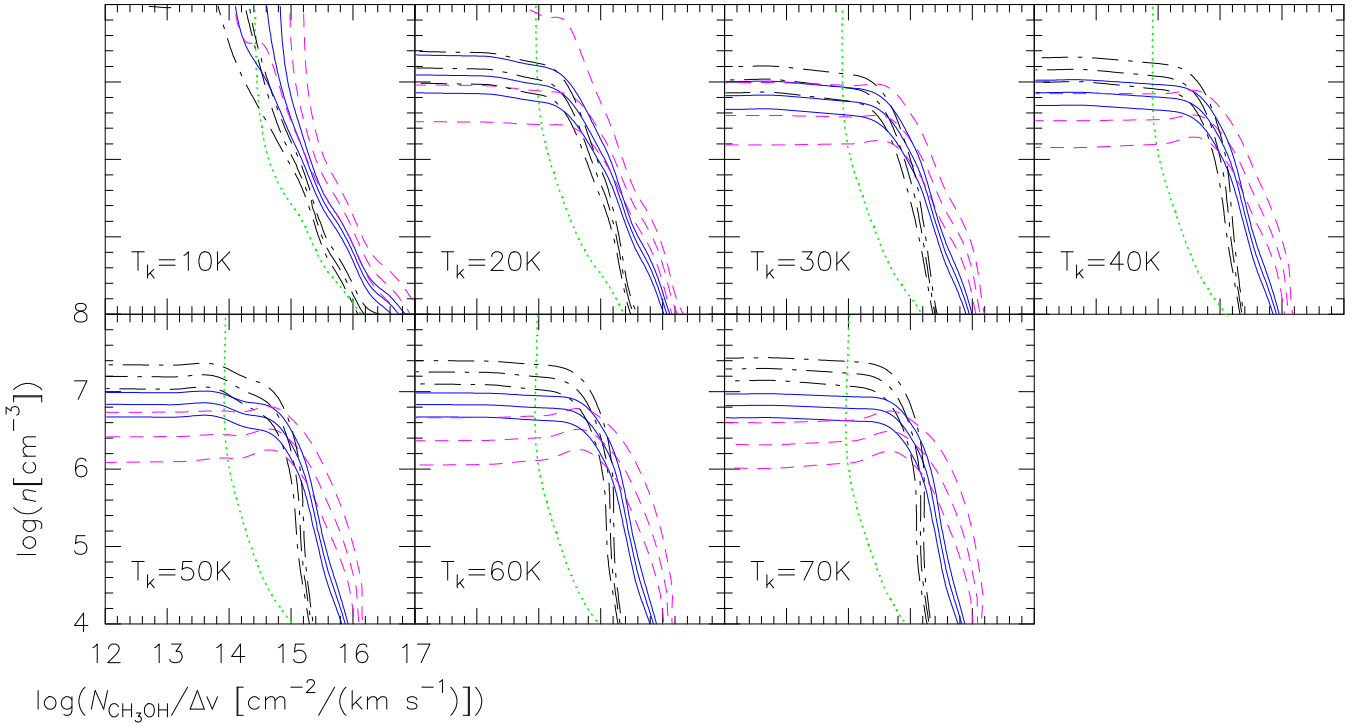


Fig. 8. Results of statistical equilibrium calculations for $\text{CH}_3\text{OH-E}$. Observed integrated intensity line ratios are color-coded as in Fig. 7 and plotted in logarithmic scale (along with their 1σ values) as function of H_2 density and $N_{\text{CH}_3\text{OH}}/\Delta v$ at different temperatures (10–70 K). The green dotted line represents the peak main brightness temperature of the $5_0 \rightarrow 4_0 E$ transition.

analysis because of the limited number of observed transitions, we can exclude the low temperature solution and put a lower limit to the kinetic temperature of the gas to 30 K. This result is in agreement with the detection of methanol maser from this region and with a previous measurement of $T = 60$ K from NH_3 observations. Therefore, we adopt $T = 60$ K as kinetic temperature at the peak of the continuum emission.

3.3. PdBI+30m: extended CH_3OH emission

A comparison of the interferometric data with the single-dish observations shows that only $\sim 30\%$ of the $\text{CH}_3\text{OH } 2_k \rightarrow 1_k$ measured with the 30 m telescope is imaged in the PdBI observations. The combined PdBI and 30 m telescope data recover almost 100 % of the flux at the central ($1''.5, 0''$) position. In Fig. 9, we show the resultant map after combining the $\text{CH}_3\text{OH } 2_k \rightarrow 1_k$ single-dish observations with the corresponding PdBI data. The methanol emission is extended already in the interferometric observations (mapping angular scales as large as $32''.5$) and confirmed to be so in the resultant merged map with the single-dish data. It is important to note that the emission is extending over 1 pc scale in the merged map (see Fig. 9). Similarly, silicon monoxide (SiO) was found to be widespread over a 2 pc scale in the IRDC G035.39-00.33 (Jiménez-Serra et al. 2010). The $2_1 \rightarrow 1_1 E$ transition was not detected in the single-dish observations, which is expected since this emission does not appear to be extended in our interferometric data.

As for the 1mm data, the missing flux in the interferometric observations is $\sim 70\%$. In the 1 mm single-dish observations, two of the strongest transitions showed up, namely: the $5_{-1} \rightarrow 4_{-1} E$ and the $5_0 \rightarrow 4_0 A$ lines. Both lines are above 3σ noise level at 6 positions out of 144 observed positions.

How is the derivation of column densities and rotational temperatures affected by missing flux? Using the combined data at

3 mm only, the slope, i.e., the rotational temperature, in the rotational diagram is not affected, within the errors, while CH_3OH column densities are higher by a factor of two.

4. Discussion

4.1. Properties of G11.11P1 compared to other cores

Despite the fact that our interferometric observations have enough sensitivity to resolve the Jeans mass ($1.8 M_\odot$) at 1 mm, the angular resolution ($2''.6 \times 1''.1$) is smaller than but very close to the Jeans length of $3''.2$ (0.05 pc). Therefore, it is difficult to conclude whether G11.11P1 does fragment or not into condensations (referred as substructures within the cores) as is often found when zooming into these cores (e.g., Zhang et al. 2009; Bontemps et al. 2010). If G11.11P1 does not fragment would mean that it has already accumulated most of its mass that will go into the final star even though $\sim 75\%$ of the (dust) emission is filtered out by the interferometer. With higher angular resolution observations, it will be possible to support either possibilities.

The virial parameter of G11.11P1 obtained by Pillai et al. (2006a), from single-dish NH_3 and dust continuum (at $870 \mu\text{m}$) observations, is unity on the scale of ~ 0.9 pc. Although, in the present work, we find that M_{vir} is much larger than the M_g on the scale of ~ 0.1 pc which would indicate that gravity is not the dominant force (Bertoldi & McKee 1992). We caution, however, that the high value of the virial parameter ($\alpha_{\text{vir}} = 3.6$) could be due to the missing flux in the interferometric data and to the fact that the virial mass is estimated from the C^{34}S line width, whose broadening is likely in part produced by outflows. In fact, Pillai et al. (2006b) reported an increase in line widths, from 1.29 km s^{-1} in the $\text{NH}_3 (1,1)$ line to 3.2 km s^{-1} in the $\text{NH}_3 (3,3)$ data. The increase in NH_3 line width toward the higher (J, K) transitions suggest a strong influence of star forming activity on

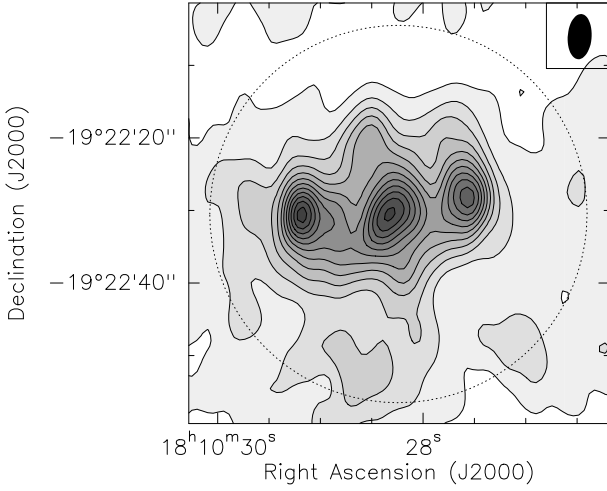


Fig. 9. $\text{CH}_3\text{OH } 2_k \rightarrow 1_k v_t = 0$ integrated intensity map combining PdBI and 30m data. The emission is integrated over the $2_{-1} \rightarrow 1_{-1}E$, $2_0 \rightarrow 1_0A$, and $2_0 \rightarrow 1_0E$ transitions. First contour and contour spacing are $0.39 \text{ Jy beam}^{-1} \text{ km s}^{-1}$ (3σ), the dashed contours show the negative emission (-3σ). The synthesized beam (6.2×3.3 ; $\text{PA} = 176^\circ$) is shown in the upper right corner. The dotted circle indicates the interferometer primary beam ($52''$).

the line width at smaller scales. The broad line width in the C^{34}S from PdBI is consistent with that notion.

Based on the SCUBA $870 \mu\text{m}$ column density, we estimated a surface density of $\Sigma = 0.4 \text{ g cm}^{-2}$ for G11.11P1, which is close to the thresholds of $0.7\text{--}1.5 \text{ g cm}^{-2}$ (or $3\,320\text{--}7\,110 M_\odot \text{ pc}^{-2}$) required to form stars of $10\text{--}200 M_\odot$ (Krumholz & McKee 2008). It is important to point out that these authors were interested in clouds where no massive stars have yet formed while G11.11P1 shows already signposts of star formation activity.

We have calculated a density profile power-law index of 1.6 from interferometric observations at 1 and 3 mm; similar values, in the range between 1.5 and 2, for cores in the IRDC G28.34+0.06, have been reported by Zhang et al. (2009) and for embedded protostellar sources in the protocluster IRAS 05358+3543 (Beuther et al. 2007) as well.

4.2. The disk/outflow system?

Pillai et al. (2006b) found a velocity gradient of the CH_3OH maser emission and explained it as the maser spots being located in a Keplerian disk. Interestingly, the spread of the maser components is in the North-South direction which is perpendicular to the $\text{CH}_3\text{OH } 2_k \rightarrow 1_k$ emission that we propose is originated by an outflow (in the East-West direction). The spread of the masing spots is translated into a radius of $\sim 450 \text{ AU}$ for a hypothetical disk in G11.11P1. Note that candidate disks in high-mass protostars have masses in the range $0.2\text{--}40 M_\odot$ and radii of $500\text{--}10\,000 \text{ AU}$ (Cesaroni et al. 2006). Our interferometric data set is capable of imaging the biggest disk structures, but not those inferred in Pillai et al. (2006b).

G11.11P1 has been cataloged by Cyganowski et al. (2008) as a “possible” massive young stellar object (YSO) outflow candidate. This categorization was based on the angular extent of the extended excess $4.5 \mu\text{m}$ emission, i.e., the extent of green emission in a three-color RGB image.

More evidence pointing to the presence of outflows comes from the non-Gaussian methanol line profiles (see Fig. 4 and

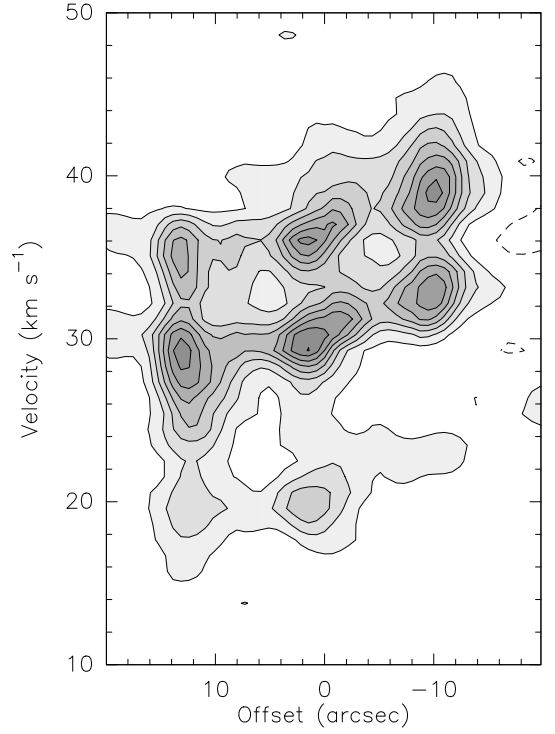


Fig. 10. Position-velocity plot of the methanol $2_k \rightarrow 1_k$ lines, cutting along the $\text{PA}=96^\circ$ on the map shown in the *middle bottom* panel of Fig. 4. Shown are the transitions: $2_{-1} \rightarrow 1_{-1}E$, $2_0 \rightarrow 1_0A$, and $2_1 \rightarrow 1_1E$. The offset is measured positive towards East and from the pointing center of the observations. First contour is 0.018 in steps of $0.036 \text{ Jy beam}^{-1} \text{ km s}^{-1}$, the dashed contours show the negative emission ($-0.018 \text{ Jy beam}^{-1} \text{ km s}^{-1}$).

Leurini et al. 2007b). In Fig. 10, we analyze the molecular emission in a position-velocity plot and note that there are “wings” of redshifted emission towards negative offsets and blueshifted emission towards positive offsets (see also Fig. 4). Moreover, we find a gradient of $\sim 4 \text{ km s}^{-1}$, in the east-west direction, for the $\text{CH}_3\text{OH } 2_k \rightarrow 1_k$ emission and speculate, it is due to an outflow(s)-cloud interaction. The $\text{C}^{34}\text{S } 2 \rightarrow 1$ and $\text{CH}_3\text{OH } 5_k \rightarrow 4_k$ lines are detected mainly towards the central peak/dust emission, and no velocity gradient is found.

Another possibility is that the $\text{CH}_3\text{OH } 2_k \rightarrow 1_k$ emission is actually tracing a toroid (see Cesaroni et al. 2007) like in the interferometric observations of $\text{CH}_3\text{OH } 6_0 \rightarrow 5_0$ towards the IRDC 18223-3 (Fallscheer et al. 2009). However, the gradient of the maser spots is orthogonal and not aligned with the gradient of the methanol emission we present in Fig. 10.

4.3. CH_3OH abundances

Due to the fact that methanol molecules can be sub-thermally excited (Bachiller et al. 1995), the temperatures derived from the rotational diagram are low ($\sim 15 \text{ K}$) even at the central peak where masers have been detected. To overcome this issue we have used the LVG method and found that a higher temperature is more reliable.

Purely gas-phase model calculations predict $X_{\text{CH}_3\text{OH}}$ to be of the order $10^{-13}\text{--}10^{-10}$ (Garrod et al. 2006), which cannot reproduce the high values we report in this paper. Garrod et al. (2006) conclude that the production of methanol is carried out on the surfaces of dust grains followed by desorption into the gas. Then

the $X_{\text{CH}_3\text{OH}}$ values in G11.P11 could be produced by desorption of icy mantles on the dust grains.

As found in Sect. 3.2.2, the highest $X_{\text{CH}_3\text{OH}}$ in G11.11P1 is at the central position ($X_{\text{CH}_3\text{OH}} \sim 3 \times 10^{-8}$), and it decreases by more than one order of magnitude at the other two peaks, where the $X_{\text{CH}_3\text{OH}}$ ($\sim 4 - 6 \times 10^{-9}$); the same trend was found also by LVG-modeling of single-dish data (Leurini et al. 2007b). Our abundances are enhanced compared to dark clouds values ($X_{\text{CH}_3\text{OH}} \sim 10^{-10} - 10^{-9}$; Friberg et al. 1988), also supporting the idea that methanol in G11.11P1 is forming mainly through non-thermal desorption by the presence of outflow(s).

5. Summary

We have performed continuum and line observations with the PdBI towards the IRDC core G11.11P1. Our main results can be summarized as follows:

- The analysis of the mm continuum maps provides a very detailed physical structure of the core.
- Evidence of extended 4.5 μm emission, “wings” in the $\text{CH}_3\text{OH } 2_k \rightarrow 1_k$ spectra, and CH_3OH abundance enhancement point to the presence of an outflow in the East-West direction.
- We find a gradient of $\sim 4 \text{ km s}^{-1}$ for the $\text{CH}_3\text{OH } 2_k \rightarrow 1_k$ emission, which we interpret as being produced by an outflow(s)-cloud interaction.
- The fitting results show enhanced methanol fractional abundance ($\sim 3 \times 10^{-8}$) at the central peak with respect to the other two maxima where the methanol abundance is lower by about an order of magnitude ($\sim 4-6 \times 10^{-9}$).

Acknowledgements. We acknowledge the IRAM staff at Pico Veleta and Plateau de Bure for carrying out the observations. L.G. thanks A. Castro-Carrizo and J. M. Winters for their help during the PdBI data reduction. We thank B. Parise for her evaluation on the manuscript and the referee for providing helpful comments and suggestions. L. G. was supported for this research through a stipend from the International Max Planck Research School (IMPRS) for Astronomy and Astrophysics at the Universities of Bonn and Cologne. T. P. acknowledges support from the Combined Array for Research in Millimeter-wave Astronomy (CARMA), which is supported by the National Science Foundation through grant AST 05-40399.

References

Aguirre, J. E., Ginsburg, A. G., Dunham, M. K., et al. 2011, *ApJS*, 192, 4
 Bachiller, R., Liechti, S., Walmsley, C. M., & Colomer, F. 1995, *A&A*, 295, L51
 Beckwith, S. V. W. & Sargent, A. I. 1991, *ApJ*, 381, 250
 Beckwith, S. V. W., Sargent, A. I., Chini, R. S., & Guesten, R. 1990, *AJ*, 99, 924
 Bertoldi, F. & McKee, C. F. 1992, *ApJ*, 395, 140
 Beuther, H., Leurini, S., Schilke, P., et al. 2007, *A&A*, 466, 1065
 Bontemps, S., Motte, F., Csengeri, T., & Schneider, N. 2010, *A&A*, 524, A18+
 Carey, S. J., Clark, F. O., Egan, M. P., et al. 1998, *ApJ*, 508, 721
 Carey, S. J., Feldman, P. A., Redman, R. O., et al. 2000, *ApJ*, 543, L157
 Cesaroni, R., Galli, D., Lodato, G., Walmsley, C. M., & Zhang, Q. 2007, *Protostars and Planets V*, 197
 Cesaroni, R., Galli, D., Lodato, G., Walmsley, M., & Zhang, Q. 2006, *Nature*, 444, 703
 Cummins, S. E., Linke, R. A., & Thaddeus, P. 1986, *ApJS*, 60, 819
 Cyganowski, C. J., Whitney, B. A., Holden, E., et al. 2008, *AJ*, 136, 2391
 Egan, M. P., Shipman, R. F., Price, S. D., et al. 1998, *ApJ*, 494, L199
 Fallscheer, C., Beuther, H., Zhang, Q., Keto, E., & Sridharan, T. K. 2009, *A&A*, 504, 127
 Friberg, P., Hjalmarson, A., Madden, S. C., & Irvine, W. M. 1988, *A&A*, 195, 281
 Garay, G., Mardones, D., Rodríguez, L. F., Caselli, P., & Bourke, T. L. 2002, *ApJ*, 567, 980
 Garrod, R., Park, I. H., Caselli, P., & Herbst, E. 2006, *Chemical Evolution of the Universe*, *Faraday Discussions*, volume 133, 2006, p.51, 133, 51
 Goldreich, P. & Kwan, J. 1974, *ApJ*, 189, 441

Goldsmith, P. F. & Langer, W. D. 1999, *ApJ*, 517, 209
 Guilloteau, S., Delannoy, J., Downes, D., et al. 1992, *A&A*, 262, 624
 Henning, T., Linz, H., Krause, O., et al. 2010, *A&A*, 518, L95
 Hildebrand, R. H. 1983, *QJRAS*, 24, 267
 Jiménez-Serra, I., Caselli, P., Tan, J. C., et al. 2010, *MNRAS*, 406, 187
 Kauffmann, J., Bertoldi, F., Bourke, T. L., Evans, II, N. J., & Lee, C. W. 2008, *A&A*, 487, 993
 Kristensen, L. E., van Dishoeck, E. F., van Kempen, T. A., et al. 2010, *A&A*, 516, A57
 Krumholz, M. R. & McKee, C. F. 2008, *Nature*, 451, 1082
 Leurini, S., Beuther, H., Schilke, P., et al. 2007a, *A&A*, 475, 925
 Leurini, S., Schilke, P., Menten, K. M., et al. 2004, *A&A*, 422, 573
 Leurini, S., Schilke, P., Wyrowski, F., & Menten, K. M. 2007b, *A&A*, 466, 215
 Looney, L. W., Mundy, L. G., & Welch, W. J. 2003, *ApJ*, 592, 255
 MacLaren, I., Richardson, K. M., & Wolfendale, A. W. 1988, *ApJ*, 333, 821
 Mathis, J. S., Rimpl, W., & Nordsieck, K. H. 1977, *ApJ*, 217, 425
 Müller, H. S. P., Schlöder, F., Stutzki, J., & Winnewisser, G. 2005, *Journal of Molecular Structure*, 742, 215
 Müller, H. S. P., Thorwirth, S., Roth, D. A., & Winnewisser, G. 2001, *A&A*, 370, L49
 Natta, A., Testi, L., Neri, R., Shepherd, D. S., & Wilner, D. J. 2004, *A&A*, 416, 179
 Ossenkopf, V. & Henning, T. 1994, *A&A*, 291, 943
 Perault, M., Omont, A., Simon, G., et al. 1996, *A&A*, 315, L165
 Pillai, T., Wyrowski, F., Carey, S. J., & Menten, K. M. 2006a, *A&A*, 450, 569
 Pillai, T., Wyrowski, F., Menten, K. M., & Krügel, E. 2006b, *A&A*, 447, 929
 Rathborne, J. M., Jackson, J. M., Chambers, E. T., et al. 2005, *ApJ*, 630, L181
 Rathborne, J. M., Jackson, J. M., Zhang, Q., & Simon, R. 2008, *ApJ*, 689, 1141
 Schuster, K., Boucher, C., Brunswig, W., et al. 2004, *A&A*, 423, 1171
 Stahler, S. W. & Palla, F. 2005, *The Formation of Stars*, ed. Stahler, S. W. & Palla, F.
 Turner, B. E. 1991, *ApJS*, 76, 617
 van der Tak, F. F. S., van Dishoeck, E. F., & Caselli, P. 2000, *A&A*, 361, 327
 Wang, Y., Zhang, Q., Rathborne, J. M., Jackson, J., & Wu, Y. 2006, *ApJ*, 651, L125
 Zhang, Q., Wang, Y., Pillai, T., & Rathborne, J. 2009, *ApJ*, 696, 268